A Technique for Retrieving the Exospheric Number Density Distribution from Pickup Ion Ring Distributions

Kei Masunaga, Naoki Terada, François Leblanc, Yuki Harada, Takuya Hara, Shotaro Sakai, Shoichiro Yokota, Kanako Seki, Atsushi Yamazaki, James P Mcfadden, et al.

The Planetary Science Journal, 5:180 (9pp), 2024 August https://doi.org/10.3847/PSJ/ad65d4

A Technique for Retrieving the Exospheric Number Density Distribution from Pickup Ion Ring Distributions

Kei Masunaga[1], Naoki Terada[2], François Leblanc[3], Yuki Harada[4], Takuya Hara[5], Shotaro Sakai[2,6], Shoichiro Yokota[7], Kanako Seki[8], Atsushi Yamazaki[9], James. P. McFadden[5], and Tomohiro Usui[9]
[1] Institute of Arts and Sciences, Yamagata University, Yamagata, Japan; kei.masunaga@cc.yamagata-u.ac.jp
[2] Department of Geophysics, Graduate School of Science, Tohoku University, Sendai, Japan
[3] LATMOS/IPSL, Sorbonne Universite, UVSQ, CNRS, Paris, France
[4] Department of Geophysics, Graduate School of Science, Kyoto University, Kyoto, Japan
[5] Space Science Laboratory, University of California Berkeley, California, USA
[6] Planetary Plasma and Atmospheric Research Center, Tohoku University, Sendai, Japan
[7] Graduate School of Science, Osaka University, Osaka, Japan
[8] Graduate School of Earth and Planetary Science, University of Tokyo, Tokyo, Japan
[9] Institute of Space and Astronautical Science, Japan Aerospace Exploration Agency, Sagamihara, Japan
Received 2024 April 1; revised 2024 June 24; accepted 2024 July 18; published 2024 August 23

Abstract

Ion pickup by the solar wind is ubiquitous in space plasma. Because pickup ions are originally produced by ionization of an exospheric neutral atmosphere, their measurements contain information on the exospheric neutral abundance. Here we established a method to retrieve exospheric number densities, by analyzing the ion velocity distribution functions of pickup ions measured by the Mars Atmosphere and Volatile EvolutioN spacecraft. We successfully retrieved exospheric oxygen density distributions at altitudes ranging from 1000 to 10,000 km around Mars except for the vicinity of the bow shock. This method can be applied to other space missions to study the upper atmosphere of planets, moons, and other small bodies in our solar system, where pickup ions exist.

Unified Astronomy Thesaurus concepts: Mars (1007); Pickup ions (1239); Planetary magnetospheres (997); Exosphere (499); Solar wind (1534)

1. Introduction

The exosphere is the outermost component of the planetary atmosphere. On Mars, it extends beyond the induced magnetosphere and is directly exposed to the solar wind. One of the major exospheric components of Mars is oxygen atoms that are created by dissociative recombination of O_2^+ in the ionosphere (e.g., Leblanc et al. 2017; Lillis et al. 2017). Once the oxygen atoms are ionized by the solar UV radiation, charge exchange, or electron impact of the solar wind, they are accelerated by the motional electric field, $\boldsymbol{E}_{\rm mot} = -\boldsymbol{v} \times \boldsymbol{B}$, and escape the planet (e.g., Dong et al. 2015). Here, $\boldsymbol{v}$ and $\boldsymbol{B}$ denote the solar wind velocity and interplanetary magnetic field vectors, respectively. This ion acceleration process is referred to as "ion pickup" and the accelerated ions are called "pickup ions." This is an important ion removal process in the Martian atmosphere and has been extensively studied through ion measurements obtained from several spacecraft. It is known that the escape flux of the pickup ions changes depending on the solar wind, solar radiation flux, and seasons (Futaana et al. 2008; Nilsson et al. 2011; Ramstad et al. 2015; Yamauchi et al. 2015; Dong et al. 2023).

To understand the ion escape process in the Martian atmosphere, it is also important to comprehend the temporal and spatial variabilities of the exospheric distributions, as the exosphere is the source of the escaping ions. However, direct measurement of the tenuous atmosphere using particle detectors is challenging. Thus, the exosphere has primarily been examined by using optical instruments, such as UV spectrographs (e.g., Anderson & Hord 1971; Feldman et al. 2000; Leblanc 2006; Chaufray et al. 2008; Deighan et al. 2015; Chaffin et al. 2018; Masunaga et al. 2020, 2022; Chirakkil et al. 2024; Susarla et al. 2024).

Rahmati (2016) and Rahmati et al. (2015, 2017, 2018) established a method for retrieving exospheric H and O number density profiles from pickup ion measurements obtained by the Mars Atmosphere and Volatile EvolutioN (MAVEN) spacecraft. They also calculated the H and O escape rates and found that although the H escape rate exhibits seasonal variations, the O escape rate does not. However, this method has only been applied to the solar wind region (>3000 km). Additionally, the hot O densities were determined based on the flux ratio of the observed pickup ions and the modeled ones that originated from a spherically symmetric O exospheric model, indicating that the retrieved O densities were highly dependent on the exospheric model used as the input.

In this study, we established a retrieval method that extends the density distribution down to the magnetosheath (∼1000 km) by analyzing the initial phase of the pickup ion ring distributions. This corresponds to the pickup ions being accelerated nearly along the motional electric field to the spacecraft. By analyzing a number of ring distributions observed not only in the solar wind but also in the magnetosheath, the 3D density distribution around Mars can be obtained. Section 2 briefly describes the instruments used in this study and illustrates how the atomic oxygen density can be retrieved at approximate pickup locations by applying Liouville's theorem to O^+ pickup ions in the initial phase of the ring distribution. Thereafter, two retrieval results for two orbits are presented in Section 3, which are then discussed and summarized in Section 4.

2. Instruments and Methods

2.1. Instruments

We used the data obtained from the SupraThermal And Thermal Ion Composition (STATIC) instrument installed on MAVEN (McFadden et al. 2015). STATIC is an energy and mass spectrometer comprising an electrostatic ion energy-to-charge analyzer and a time-of-flight mass-to-charge analyzer. It measures 3D ion velocity distribution functions across an energy range of 0.1–30 keV and a field of view of 360° (azimuth) × 90° (elevation). In this study, we used the "d1" data product comprising 32 energy, 8 mass, 16 azimuth, and 4 elevation bins. We also used data obtained from the Solar Wind Ion Analyzer (SWIA), magnetometer (MAG), Solar Wind Electron Analyzer (SWEA), and Extreme Ultraviolet Monitor (EUVM) to calculate the motional electric field and ionization rates of O atoms. The details of these instruments have been explained by Connerney et al. (2015), Halekas et al. (2015), Mitchell et al. (2016), and Eparvier et al. (2015).

2.2. Methods

We analyzed O^+ ion velocity distribution functions (VDFs) measured by STATIC to retrieve the Martian exospheric O densities. In collisionless plasma, pickup ions exhibit an $E \times B$ drift motion. When the magnetic field and the electric field point to the y- and the z-axes in a rest frame, respectively, the motion of the $E \times B$ drift lies on the xz plane as shown in Figure 1(a). The position of a pickup ion is described by cycloid motion as follows:

$$x_{\rm PUI} = x_0 + r_{\rm g}(\theta_{\rm P} - \sin\theta_{\rm P}) \quad (1)$$

$$z_{\rm PUI} = z_0 + r_{\rm g}(1 - \cos\theta_{\rm P}), \quad (2)$$

where x_0 and z_0 denote the pickup location, and $r_{\rm g}$ denotes the gyroradius of the pickup ion ($m v_{\rm SWper}/eB$, where m is ion mass, e is the elementary charge, $v_{\rm SWper}$ is the ion velocity perpendicular to the magnetic field vector, and B is the magnitude of the magnetic field). Additionally, $\theta_{\rm P}$ denotes the phase angle, which corresponds $\omega_{\rm g} t$, where $\omega_{\rm g}$ is the gyrofrequency and t is the time elapsed since pickup (Figure 1(b)). As $x_{\rm PUI}$ and $z_{\rm PUI}$ correspond to the spacecraft position and $r_{\rm g}$ and $\theta_{\rm P}$ can be obtained from the measured ion velocity and magnetic field vectors, we can calculate the original pickup location by assuming the pickup ions are on the initial gyromotion of the $E \times B$ drift as follows:

$$x_0 = x_{\rm PUI} - r_{\rm g}(\theta_{\rm P} - \sin\theta_{\rm P}) \quad (3)$$

$$z_0 = z_{\rm PUI} - r_{\rm g}(1 - \cos\theta_{\rm P}). \quad (4)$$

In the velocity space, cycloid motion is described as a ring distribution as shown in Figure 1(b) (also see Dubinin et al. 2006; Coates & Jones 2009; Masunaga et al. 2016; Rahmati 2016; Masunaga et al. 2017; Lin et al. 2022). In the initial phase of the ring distribution, which is defined as one-eighth of the ring ($0° < \theta_{\rm P} < 45°$, where $\theta_{\rm P}$ is the phase angle, as shown in Figure 1(b)) in this study, pickup ions are accelerated nearly along the electric field (i.e., the angle between the ion velocity and the electric field direction is ≤ 22.5, which corresponds to a single angular width of the STATIC instrument). This motion can be approximated as a simple acceleration motion along the electric field. As illustrated in Figure 1(c), exospheric oxygen atoms are ionized at the ionization rate R; thereafter, the newly formed O^+ ions are accelerated by the motional electric field $E_{\rm mot}$ (along the z-axis) and are detected by STATIC. STATIC measures the O^+ ion phase space density (PSD) $f(W_1)$ for viewing directions of each azimuthal and elevation channel at spacecraft location ($z = z_1$) at $t = t_1$, which also provides individual O^+ ion velocity vectors and fluxes. Using Liouville's theorem, we assumed that the observed PSD is conserved from the pickup location to the observation location. This enabled us to associate the PSD measured at the spacecraft location with that at the pickup location,

$$f(z_0', W_0, t_0) = f(z_1, W_1, t_1). \quad (5)$$

Here, the pickup location is approximated as $z = z_0'$, where the newborn ions have an energy of W_0, which corresponds to half of the energy width ($= dW/2$) after ionization (at time $t = t_0$), as shown in Figure 1(d). Assuming a quasi-steady condition, Equation (1) is transformed into

$$f(z_0', W_0) = f(z_1, W_1). \quad (6)$$

The PSD and measured differential particle flux J are related as follows (Baumjohann & Treumann 2012):

$$f = \frac{m^2}{2W} J, \quad (7)$$

where m and W denote the mass and energy of the particle, respectively. Given that the pickup ions in the initial phase of the ring distribution are accelerated nearly along the electric field, Equations (6) and (7) result in the differential particle flux at the pickup location $z = z_0'$:

$$J_0 = \frac{W_0}{W_1} J_1. \quad (8)$$

We assume that the number of O^+ ions with energy of W_0 in the volume dV_0 ($= dAdz$, where dA indicates the instrumental effective area) is equal to the number of O^+ ions produced by the ionization of O atoms at the pickup location:

$$n_{\rm O} R dV_0 dt = J_0 dW d\Omega dA dt, \quad (9)$$

which leads to

$$n_{\rm O} = \frac{\frac{W_0}{W_1} J_1 dW d\Omega}{R dz} = \frac{J_1 dW d\Omega}{2R z_1}, \quad (10)$$

where $dz = dW/e|\boldsymbol{E}_{\rm mot}|$, $W_0 = dW/2$, and $W_1 = e|\boldsymbol{E}_{\rm mot}|z_1$. Note that z_1 is the distance along which the O^+ ions are accelerated by the electric field. The ionization rate of O atoms is expressed as

$$R = R_{\rm PI} + R_{\rm CX} + R_{\rm EI}, \quad (11)$$

where $R_{\rm PI}$, $R_{\rm CX}$, and $R_{\rm EI}$ are the photoionization, charge exchange ionization, and electron impact ionization rates, respectively, which are calculated as

$$R_{\rm PI} = \int_\lambda \sigma_{\rm PI}(\lambda) F(\lambda) d\lambda \quad (12)$$

$$R_{\rm CX} = \sigma_{\rm CX} n_{\rm SW} v_{\rm SW} \quad (13)$$

$$R_{\rm EI} = \int_{\rm E} \sigma_{\rm EI}(W) F_{\rm e}(W) dW, \quad (14)$$

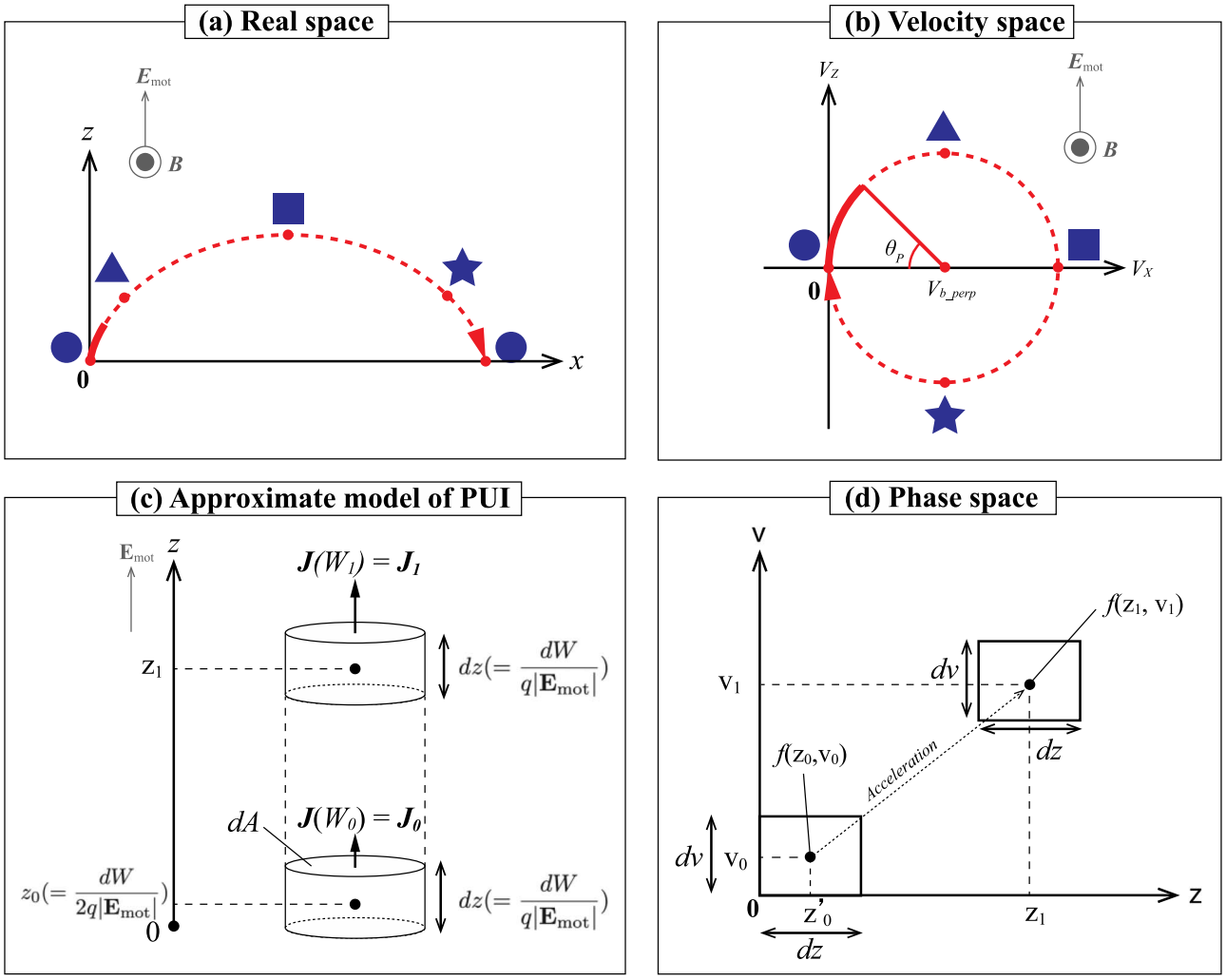

Figure 1. Motion of a pickup ion in the real space ($E \times B$ drift). (b) Distribution of pickup ions in the velocity space (ring distribution). (c) Approximate motion of pickup ions in the initial phase of the ring distribution. (d) Acceleration of pickup ions in the phase space.

where σ_{PI}, σ_{CX}, and σ_{EI} are the cross sections of photoionization, charge exchange, and electron impact, respectively; $F(\lambda)$ is the solar flux; n_{SW} and v_{SW} are the solar wind proton density and velocity, respectively; and $F_e(W)$ is the omnidirectional electron differential flux (Rahmati 2016; Rahmati et al. 2017). We calculated these ionization rates based on the locally obtained EUVM, SWIA, and SWEA measurements. These rates could significantly differ between the spacecraft and the pickup locations. We discuss this effect by comparing the locally calculated ionization rates with statistically calculated ionization rates in Section 4.

J_1 and W_1 were measured by STATIC and $\boldsymbol{E}_{mot}(= -\boldsymbol{v} \times \boldsymbol{B})$ by SWIA and MAG. Note that we only used data outside the ion composition boundary defined by $\boldsymbol{r} = \frac{n_{O+} + n_{O2+}}{n_{H+}} < 1$ (Matsunaga et al. 2017); therefore, protons were dominant species in the STATIC VDF, and the observed plasma bulk velocity corresponded to the solar wind or magnetosheath velocity. R_{PI}, R_{CX}, and R_{EI} were calculated using the solar UV flux measurements performed by EUVM, solar wind's proton density and velocity by SWIA, and electron fluxes by SWEA. Using these measurements and Equation (10), we calculated the exospheric O density at the pickup locations. By repeating this calculation for every ion measurement in the initial phase of the ring distribution, we obtained the spatial distribution of the exospheric O density nearly along the MAVEN orbit.

The error of each retrieved density was also evaluated using the standard deviations of O^+ differential particle flux (ΔJ_1), ionization rates (ΔR), and the accelerated distance (Δz_1),

$$n_O \pm \Delta n_O = \frac{(J_1 \pm \Delta J_1) dW d\Omega}{2(R \pm \Delta R)(z_1 \pm \Delta z_1)}, \tag{15}$$

where Δn_O is calculated by considering the propagation of error:

$$\Delta n_O = \frac{dW d\Omega}{2} \sqrt{\left(\frac{\Delta J_1}{R z_1}\right)^2 + \left(\frac{J_1}{R^2 z_1^2} \sqrt{(z_1 \Delta R)^2 + (R \Delta z_1)^2}\right)^2}. \tag{16}$$

ΔJ_1 was calculated based on the square root of O^+ ion counts in each bin of the d1 data. ΔR was calculated by $\Delta R = \sqrt{\Delta R_{PI}^2 + \Delta R_{CX}^2 + \Delta R_{EI}^2}$, where ΔR_{PI}, ΔR_{CX}, and ΔR_{EI} are the standard deviation of each ionization rate during a single ion VDF observation time. Δz_1 was calculated by the error of Equation (4). That corresponds to $\Delta r_g(1 - \cos\theta_P)$,

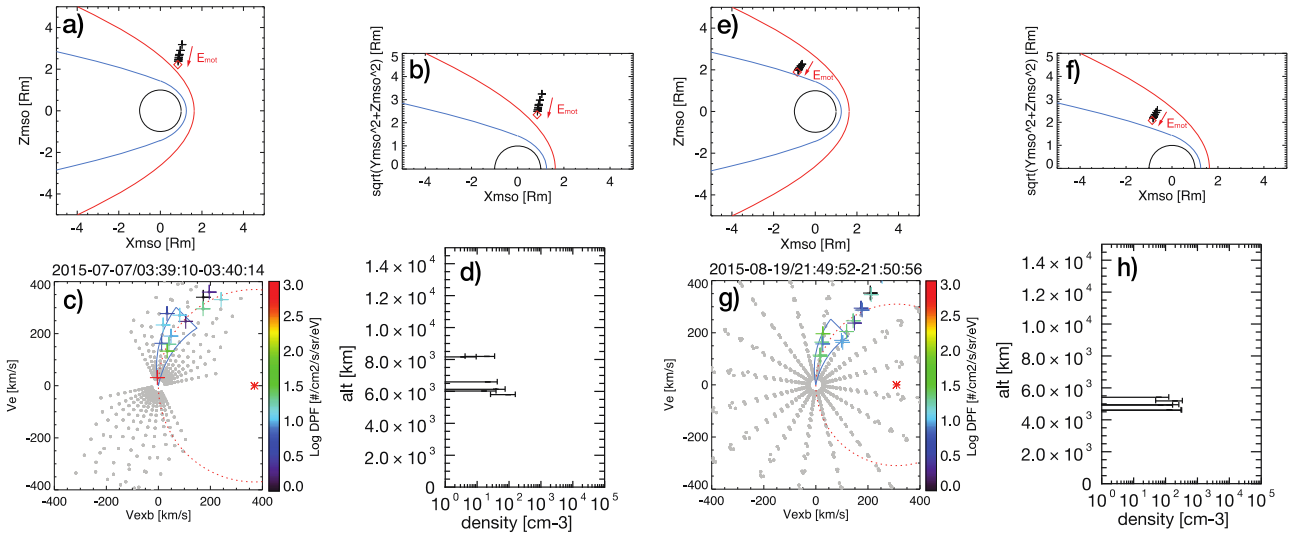

Figure 2. MAVEN position where pickup O^+ ions were observed in the solar wind (red diamonds) in the (a) *XZ* and (b) cylindrical planes of the Mars-centered Solar Orbital (MSO) coordinate system. The pickup locations of these pickup ions are denoted by the black "+" symbols. (c) O^+ ion differential particle fluxes (DPFs) are projected onto the plane perpendicular to the local magnetic field. The dotted red curve indicates the expected ring distribution calculated using the local proton velocity and magnetic field vectors. The initial phase of the ring distribution is bound by the blue curves. The gray filled circles indicate each data point in the field of view of STATIC in the perpendicular plane. (d) Retrieved O number densities at the pickup locations. (e)–(h) Magnetosheath measurements are shown in the same format as those in (a)–(d).

and Δr_g can be calculated using the standard deviation of the solar wind velocity and local magnetic field during a single ion VDF observation, that is $\Delta r_g = \frac{m}{e}\sqrt{\left(\frac{\Delta v_{SWper}}{B}\right)^2 + \left(\frac{v_{SWper}}{B^2}\Delta B\right)^2}$.

The retrieved O profile was then compared with the Exospheric Global Model (EGM) developed by Leblanc et al. (2017). The EGM is a 3D multispecies collisional parallelized model that traces the nonthermal particles. It uses inputs provided by the General Circulation Model of the Laboratoire de Meteorologie Dynamique (LMD-GCM) for the background atmosphere (Chaufray et al. 2014). It was also coupled with the Latmos Hybrid Simulation (LatHyS) to incorporate solar wind interactions with the upper atmosphere. In EGM, nonthermal O atoms are mainly produced by the dissociative recombination of O_2^+, with a small contribution from sputtering by incident pickup ions. We traced the nonthermal O test particles in the collisional upper atmosphere, generating a 3D nonthermal O density distribution. Using mean solar conditions at the time of the observations as inputs for the LMD-GCM and LatHyS, we generated a 3D distribution of the nonthermal O atoms for comparison with our retrieval results.

3. Results

Figures 2(a)–(d) show examples of STATIC observations in the solar wind. The red diamonds in Figures 2(a) and (b) indicate the average position of MAVEN in the solar wind from 03:39:10 UT to 03:40:14 UT on 2015 July 7. The average motional electric field calculated using the SWIA and MAG measurements is plotted by the red arrow. Additionally, STATIC observed a VDF represented by the "d1" data product. Figure 2(c) shows the average O^+ ion VDF with the expected ring distribution. Note that we only considered ions with an energy >50 eV to eliminate the effects of spacecraft potential and spacecraft velocity. We also considered ions with pitch angles of $90 \pm 22.^\circ5$ as they were almost in the plane perpendicular to the local magnetic field. As described in Section 2, we only used data from the initial phase of the ring distribution, which is bounded by blue curves ($0^\circ < \theta_P < 45^\circ$ and a velocity width of ±10%). Moreover, we discarded data wherein the number of nonzero count detections in the initial phase of the ring distribution was less than four, which was defined as noise in this study. We also discarded data obtained within 20 minutes before and after the crossings of the bow shock across which solar wind conditions and ionization rates were largely different, resulting in large errors in our retrieval results. Using these data, we retrieved the O number density at the pickup locations, as shown in Figure 2(d). Because MAVEN was situated in the −E hemisphere, wherein the motional electric field points toward the planet, these ions originated from a more distant exosphere, as shown in Figures 2(a) and (b). Figures 2(e)–(h) show examples of STATIC observations in the magnetosheath obtained from 21:49:52 UT to 21:50:56 UT on 2015 August 19. In the magnetosheath, the motional electric field formed by the shocked solar wind locally accelerates the newborn O^+ ions (Figures 2(e) and (f)). Therefore, we observed O^+ ions along the expected ring distribution in the magnetosheath as seen in Figure 2(g). Using the same approach as that for solar wind, we obtained the exospheric O density at the pickup locations in the magnetosheath (Figure 2(h)).

By repeating these retrievals for every 3D VDF, we obtained the O density distribution around the terminator for Orbit #1495, as shown in Figures 3(a)–(d). The altitudinal profiles of the retrieved O density for all data, the inbound leg, and the outbound leg are shown in Figures 3(e)–(g), wherein it is evident that the O densities were retrieved from altitudes of 1000–10,000 km. The individual measurements are indicated by light gray and their average over 400 km bins by orange. The blue crosses represent the O profile obtained at the MAVEN positions in the EGM. Although the individual data

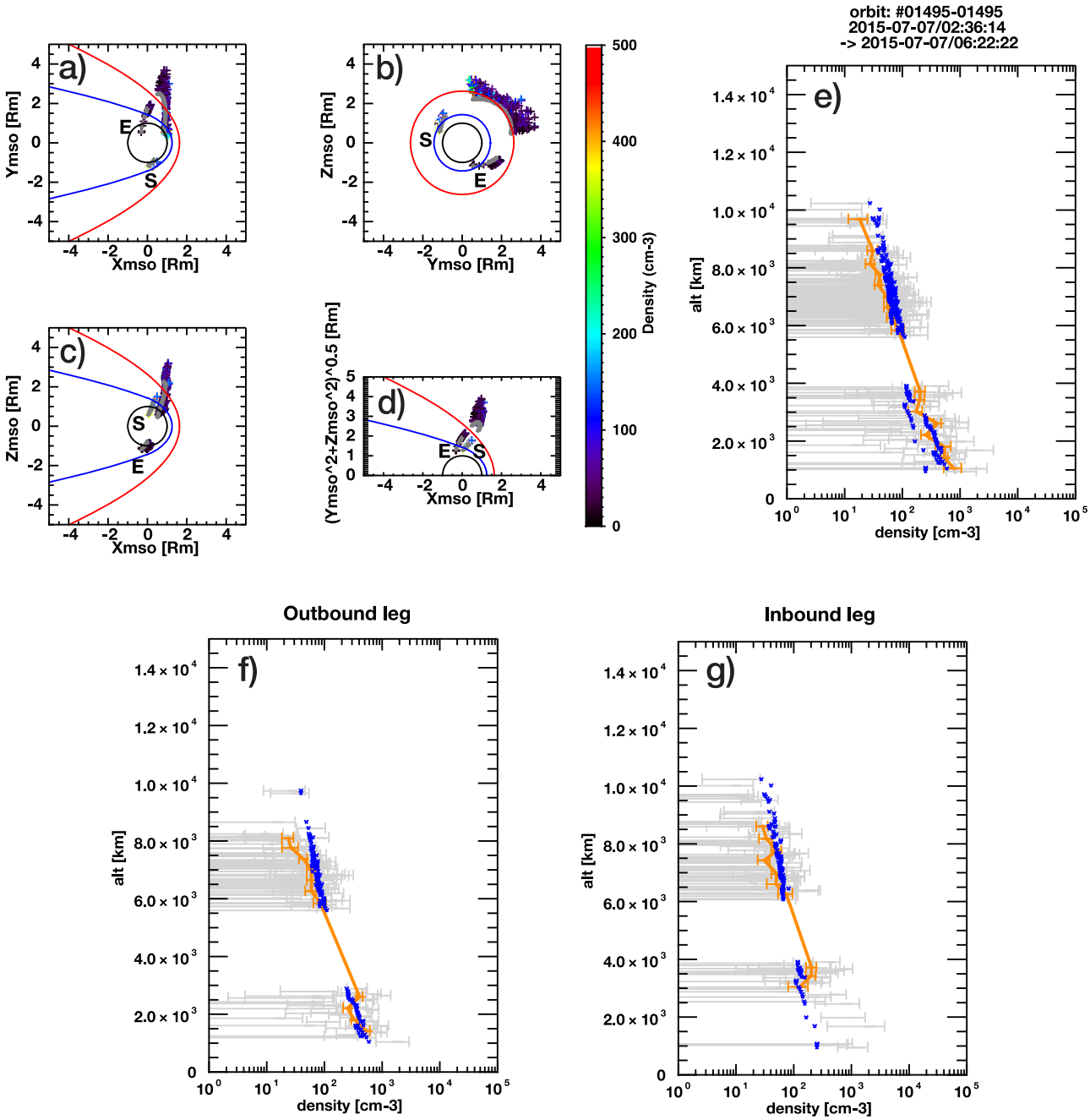

Figure 3. (a)–(d) O number density distributions retrieved along the MAVEN orbit (gray) in the MSO coordinate system. The red and blue lines correspond to the empirical model of the bow shock and induced magnetospheric boundary, respectively (Trotignon et al. 2006). "S" and "E" in these figures stand for the start and end time of the observation. (e) Altitude profiles of the retrieved O number density (gray crosses) and EGM (blue) for all data, inbound leg, and outbound leg, respectively. The orange error bars indicate the standard deviation for every 200 km bin.

has large error bars, the mean profile of our retrieval results agreed reasonably well with the EGM results.

Figure 4 shows the retrieval and EGM results for Orbit #1733, wherein the O density was retrieved from 4000 to 12,000 km altitudes, covering a wide range of the solar zenith angles near the day-to-night plane. As the EGM results look different between the inbound and outbound legs, we evaluate the retrieved results separately. For the inbound leg, the mean altitude profile of the retrieved O density agreed reasonably well with the EGM results as seen in Figure 4(g) (blue crosses). However, the retrieval results departed from the EGM results approximately below 7000 km for the outbound leg, as seen in Figure 4(f). This region mainly corresponds to the nightside magnetosheath.

4. Discussion

This study reports a method for retrieving the exospheric number density using ion measurements obtained around Mars. We analyzed the O^+ ion VDFs observed in the solar wind and the magnetosheath by MAVEN/STATIC and retrieved exospheric O densities around Mars using the measurements obtained in the initial phase of the ring distribution, where the O^+ ions are accelerated nearly along the motional electric field.

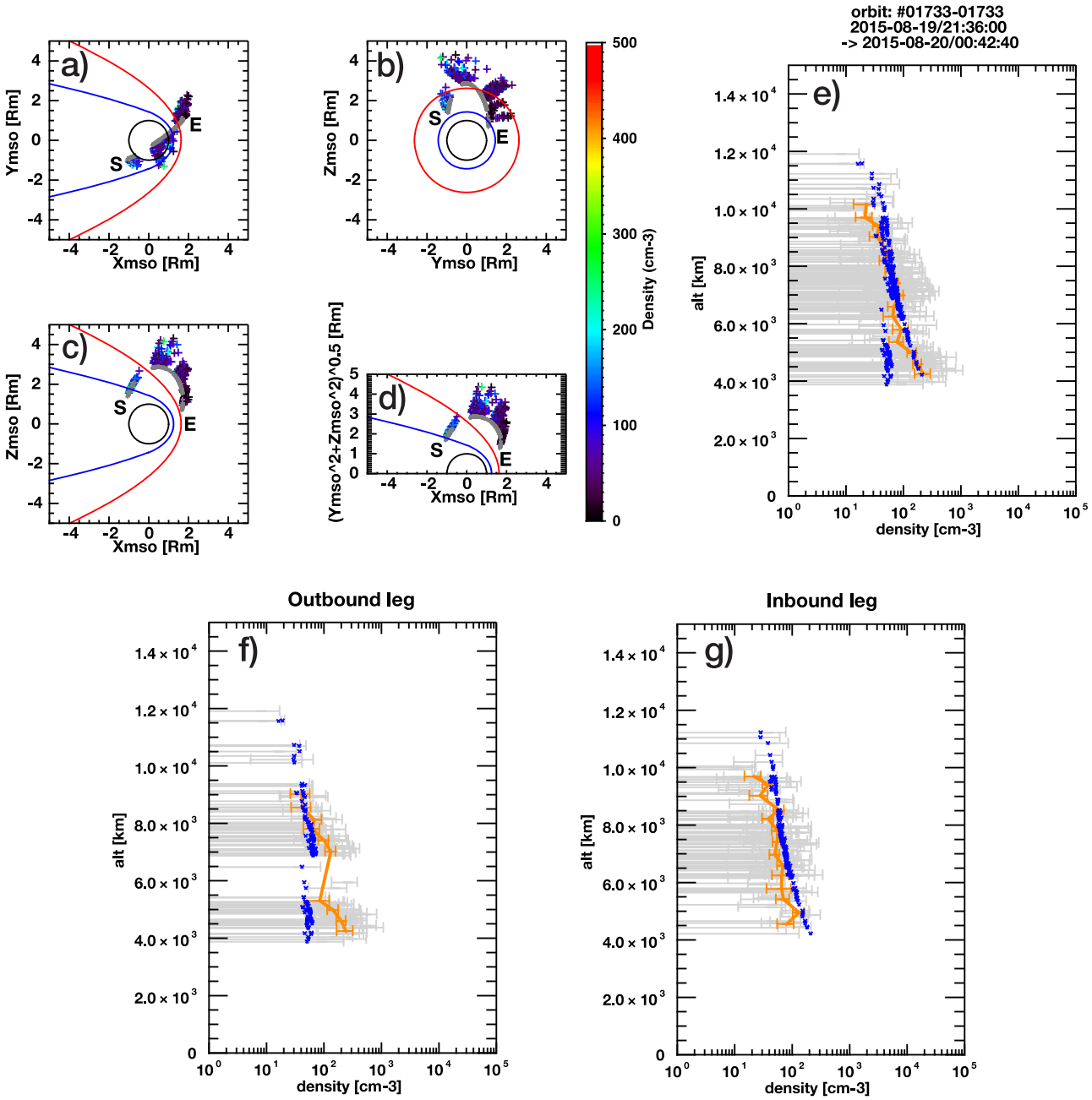

Figure 4. O number density distributions retrieved along MAVEN Orbit #1733. The format is the same as that used in Figure 3.

We applied the retrieval method to the STATIC data of two selected orbits (Orbit #1495, near the terminator plane, and Orbit #1733, near the day-to-night plane) and obtained two altitude profiles for exospheric O density. The retrieved density profiles were compared with the EGM results. Near the terminator plane, the mean number density profiles agreed reasonably well with the EGM results, although the individual data had large uncertainties. Near the day-to-night plane, the mean profile overall agreed well with the EGM result, but the retrieval results departed from the EGM results in the nightside magnetosheath. The overall consistency between the retrieved and modeled densities suggests that O atoms are mainly produced by the dissociative recombination of O_2^+ in the ionosphere (Leblanc et al. 2018). The large uncertainty can be caused by various factors, such as the temporal variations in the O^+ flux, solar UV fluxes, and the solar wind conditions (velocity, density, and magnetic field) during the integration time (64 s). Spatial variations in these values between the spacecraft and pickup locations could be another factor to cause large errors in our retrieval results.

Although we assumed that the O^+ pickup ions originated from an approximate pickup location, it is possible that they were picked up at further locations; that is, the pickup ions in the initial phase of the ring distribution could contain those picked up in subsequent gyrations. Note that O^+ gyroradius can be approximately calculated by $167 \times \frac{V_{\rm per}[{\rm km/s}]}{B\,[{\rm nT}]}$, and for Orbit #1495 and Orbit #1733, it is typically 14,000 km and 17,000 km in the solar wind and 3000 km and 5000 km in the magnetosheath, respectively. Regarding these orbits, however, we obtained measurements primarily from the −E hemisphere, where pickup ions produced in the distant

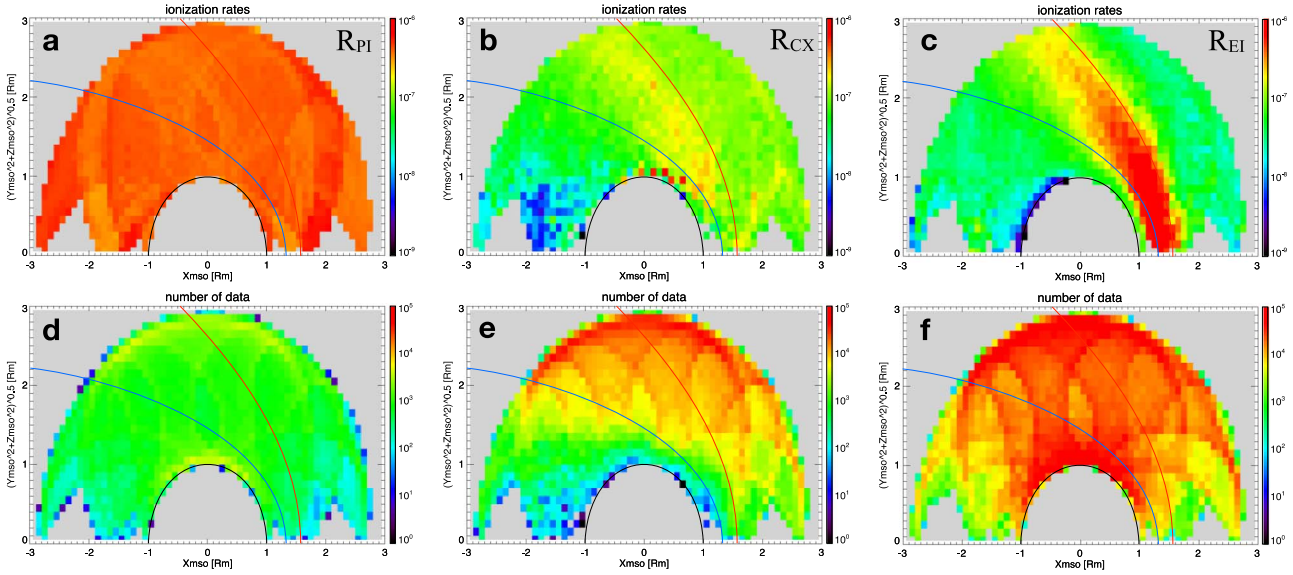

Figure 5. Spatial distributions of average ionization rates (s^{-1}) of O atoms for (a) photoionization, (b) charge exchange, and (c) electron impact based on EUVM, SWIA, and SWEA measurements, respectively, from 2014 to 2016 October. Panels (d), (e), and (f) indicate the number of measurements in each bin. The red and blue lines indicate the empirical model of the bow shock and induced magnetosphere boundary, respectively.

exosphere precipitate toward Mars. This means that local ionizations of the exospheric O are the dominant source of the observed pickup ions, and therefore, Equation (9) is thus approximately true. In contrast, in the +E hemisphere, where the motional electric field points outward from the planet, pickup ions originate from an altitude lower than the spacecraft location, such as the magnetic pileup region or the top of the ionosphere. Because of the typically large magnetic fields and low speed of the shocked solar wind in these regions, pickup ions have small gyroradii (<1000 km) and therefore undergo several gyrations before reaching the spacecraft. In this case, the initial phase of the ring distribution could contain pickup ions not only from the initial gyration but also from subsequent ones, which means that the left-hand side of Equation (9) requires another term, such as advection. To estimate this effect, a model–data comparison is required in future work.

The discrepancy between our retrieval and EGM results below 7000 km in the nightside magnetosheath may be related to the ionization rates of the O atoms, defined in Equations (12)–(14) In this study, the ionization rates of O atoms by photoionization, charge exchange, and electron impact were derived from local EUVM, SWIA, and SWEA measurements (i.e., spacecraft locations). To examine the effects of the ionization rates on the retrieved results, we also retrieved O densities based on the photoionization, charge exchange, and electron impact ionization rates that were statistically calculated using SWIA and SWEA measurements between 2014 and 2016 October. Figures 5(a)–(c) show maps of the average values in each bin on the cylindrical coordinate system. The number of data points in each bin is shown in Figures 5(d)–(f). Using the ionization rates at each pickup location during each retrieval, we obtained another retrieval result, as shown in Figure 6. For Orbit #1495, although the data cover only the lower altitudes through which MAVEN has passed, the O density distribution does not significantly change from that derived from the local ionization rates (Figures 6(a)–(c)). On the other hand, for Orbit #1733, the O density distribution in the nightside magnetosheath during the outbound leg agrees with the EGM result better than that of using local ionization rates (Figure 6(e)). The O distribution during the inbound leg in the solar wind departs from the EGM results, which means that the use of the local ionization rates is better in the solar wind (Figure 6(f)). These results suggest that our retrieval method works fine by using the local ionization rates on the dayside, but the large variations in charge exchange and electron impact ionization rates in the nightside magnetosheath, seen in Figures 5(b) and (c), highly affect our retrieval results. Statistical analysis is needed in our future study to determine the boundary across which local ionization rates or remote ionization rates should be applied.

The Martian exosphere is highly variable responding to the space weather, such as solar radiation and solar wind, and to the lower atmospheric weather, including dust storms and atmospheric waves (e.g., Lee et al. 2018, Yigit 2021; Masunaga et al. 2022). In future work, we will statistically analyze the VDFs collected by MAVEN over approximately 10 yr since its launch and build empirical models of the Martian O exosphere for different space and atmospheric weather conditions. Additionally, the proposed retrieval method can be applied to other space missions to study exospheres of various planets, moons, and small bodies in our solar system comprising pickup ions. For example, Venus has plasma and upper atmospheric environments similar to those of Mars (e.g., Futaana et al. 2017). Therefore, by applying the proposed method to VDFs measured by the Ion Mass Analyzer on Venus Express (Barabash et al. 2007), we can examine the Venusian exosphere distribution and its variations. We also aim to apply this method to the ion VDFs that will be measured by the Mass Spectrum Analyzer (MSA) on the Martian Moons Exploration mission to study the Martian exosphere and possibly the tenuous atmosphere of Martian moons (Yokota et al. 2021). The high mass resolution of MSA will allow us to study various exospheric species. Therefore, the proposed retrieval

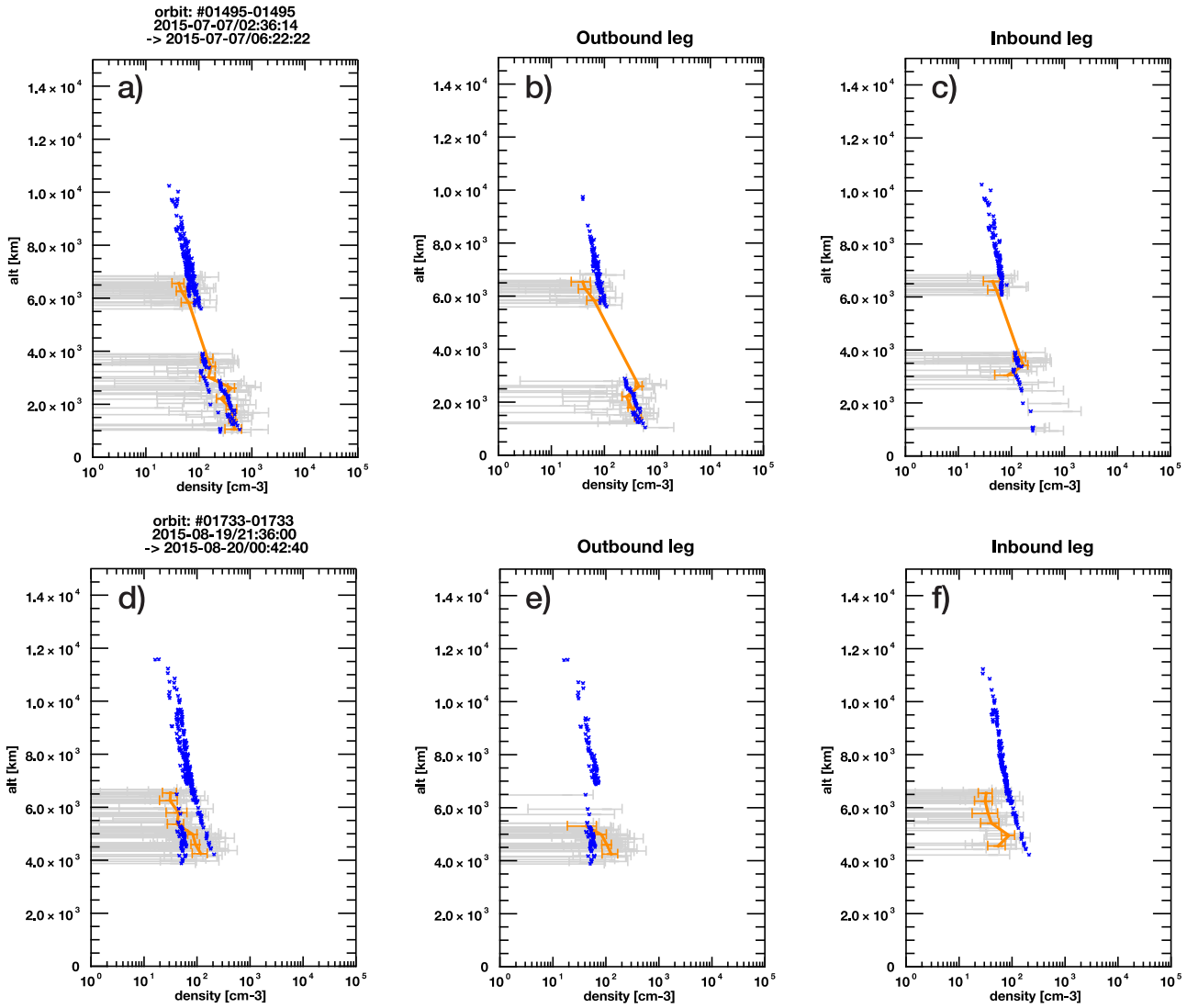

Figure 6. The O number density profiles that are retrieved from pickup ion measurements from Orbits (a) #1495 and (d) #1733 using the statistically calculated charge exchange and electron impact ionization rates as shown in Figure 5. Their outbound and inbound legs are also shown in the panels (b), (c), (e), and (f), respectively. Note that no data are plotted at the high altitudes (6500 km and higher) because MAVEN has never attained them, and no in situ SWIA and EUVM measurements have been collected.

method can be a useful "remote sensing" tool for surveying the spatial distribution and variations in the exospheres of solar system bodies.

Acknowledgments

K.M. is supported by JSPS KAKENHI (grant Nos. JP21K20387 and JP22K03708). N.T. was supported by JSPS KAKENHI grant number JP22H00164. Y.H. acknowledges support through JSPS KAKENHI Grant (JP22K14085, JP22H01285, JP22KK0045). S. S. is supported by JSPS KAKENHI (grant Nos. JP22K03695 and JP22KK0044). The MAVEN data are available in the NASA Planetary Data System.

ORCID iDs

Kei Masunaga https://orcid.org/0000-0001-9704-6993
Naoki Terada https://orcid.org/0000-0001-5685-9736
François Leblanc https://orcid.org/0000-0002-5548-3519
Yuki Harada https://orcid.org/0000-0002-4001-6352
Takuya Hara https://orcid.org/0000-0003-4605-8454
Shotaro Sakai https://orcid.org/0000-0001-9135-2076
Shoichiro Yokota https://orcid.org/0000-0001-8851-9146
Kanako Seki https://orcid.org/0000-0001-5557-9062

References

Anderson, D. E., & Hord, C. W. 1971, JGR, 76, 6666
Barabash, S., Sauvaud, J.-A., Gunell, H., et al. 2007, P&SS, 55, 1772
Baumjohann, W., & Treumann, R. A. 2012, Basic Space Plasma Physics (Revised ed.; London: Imperial College Press)
Chaffin, M. S., Chaufray, J. Y., Deighan, J., et al. 2018, JGRE, 123, 2192
Chaufray, J. Y., Bertaux, J. L., Leblanc, F., & Quemerais, E. 2008, Icar, 195, 598
Chaufray, J.-Y., Gonzales-Galindo, F., Forget, F., et al. 2014, JGRE, 119, 1614
Chirakkil, K., Deighan, J., Chaffin, M. S., et al. 2024, JGRA, 129, e2023JA032342
Coates, A. J., & Jones, G. H. 2009, P&SS, 57, 1175
Connerney, J. E. P., Espley, J., Lawton, P., et al. 2015, SSRv, 195, 257
Deighan, J., Chafin, M. S., Chaufray, J.-Y., et al. 2015, GeoRL, 42, 9009
Dong, Y., Brain, D. A., Ramstad, R., et al. 2023, Icar, 393, 115288
Dong, Y., Fang, X., Brain, D. A., et al. 2015, GeoRL, 42, 8942

Dubinin, E., Fraenz, M., Woch, J., et al. 2006, GeoRL, 33, L22103
Eparvier, F. G., Chamberlin, P. C., Woods, T. N., & Thiemann, E. M. B 2015, SSRv, 195, 293
Feldman, P. D., Burgh, E. B., Durrance, S. T., & Davidsen, A. F. 2000, ApJ, 538, 395
Futaana, Y., Barabash, S., Yamauchi, M., et al. 2008, P&SS, 56, 873
Futaana, Y., Wieser, G. S., Barabash, S., et al. 2017, SSRv, 212, 1453
Halekas, J. S., Taylor, E. R., Dalton, G., et al. 2015, SSRv, 195, 125
Leblanc, F., Chaufray, J. Y., Lilensten, J., Witasse, O., & Bertaux, J.-L. 2006, JGRE, 111, E09S11
Leblanc, F., Chaufray, J. Y., Modolo, R., et al. 2017, JGRE, 122, 2401
Leblanc, F., Martinez, F., Chaufray, J. Y., et al. 2018, GeoRL, 45, 4685
Lee, Y., Dong, C., Pawlowski, D., et al. 2018, GeoRL, 45, 6814, GeoRL
Lillis, R. J., Deighan, J., Fox, J. L., et al. 2017, JGRA, 122, 3815
Lin, H., Guo, J., Masunaga, K., et al. 2022, ApJ, 934, 183
Masunaga, K., Seki, K., Brain, D. A., et al. 2016, JGRA, 121, 3093
Masunaga, K., Seki, K., Brain, D. A., et al. 2017, JGRA, 122, 4089
Matsunaga, K., Seki, K., Brain, D. A., et al. 2017, JGRA, 122, 9723
Masunaga, K., Terada, N., Yoshida, N., et al. 2022, NatCo, 13, 6609
Masunaga, K., Yoshioka, K., Chaffin, M. S., et al. 2020, JGRE, 125, e2020JE006500
McFadden, J. P., Kortmann, O., Curtis, D., et al. 2015, SSRv, 195, 199
Mitchell, D. L., Mazelle, C., Sauvaud, J.-A., et al. 2016, SSRv, 200, 495
Nilsson, H., Edberg, N. J. T., Stenberg, G., et al. 2011, Icar, 215, 475
Rahmati, A. 2016, PhD thesis, Univ. Kansas
Rahmati, A., Larson, D. E., Cravens, T. E., et al. 2015, GeoRL, 42, 8870
Rahmati, A., Larson, D. E., Cravens, T. E., et al. 2017, JGRA, 122, 3689
Rahmati, A., Larson, D. E., Cravens, T. E., et al. 2018, JGRE, 123, 1192
Ramstad, R., Barabash, S., Futaana, Y., et al. 2015, JGRE, 120, 1298
Susarla, R., Deighan, J., Chaffin, M. S., et al. 2024, JGRA, 129, e2024JA032525
Trotignon, J. G., Mazelle, C., Bertucci, C., Acuna, M. H., et al. 2006, P&SS, 54, 357
Yamauchi, M., Hara, T., Lundin, R., et al. 2015, P&SS, 119, 54
Yigit, E. 2021, Sci, 374, 1323
Yokota, S., Terada, N., Matsuoka, A., et al. 2021, EP&S, 73, 216